Controlling Ion Uptake in Carboxylated Mixed Conductors

Zeyuan Sun[1], Mengting Sun[1], Siyu Qin[1], Meng Wang[1], Yulong Zheng[2], Brian Khau[3], Han Li[1], Thomas E. Gartner III[1], Christopher J Takacs[4*], Elsa Reichmanis[1*]

[1]Department of Chemical and Biomolecular Engineering, Lehigh University, Bethlehem, PA 18015, United States

[2]School of Chemistry and Biochemistry, Georgia Institute of Technology, Atlanta, GA 30332, United States

[3]School of Chemical and Biomolecular Engineering, Georgia Institute of Technology, Atlanta, GA 30332, United States

[4]Stanford Synchrotron Radiation Lightsource SLAC National Accelerator Laboratory, Menlo Park, CA 94025, United States

Table of Contents Graphic:

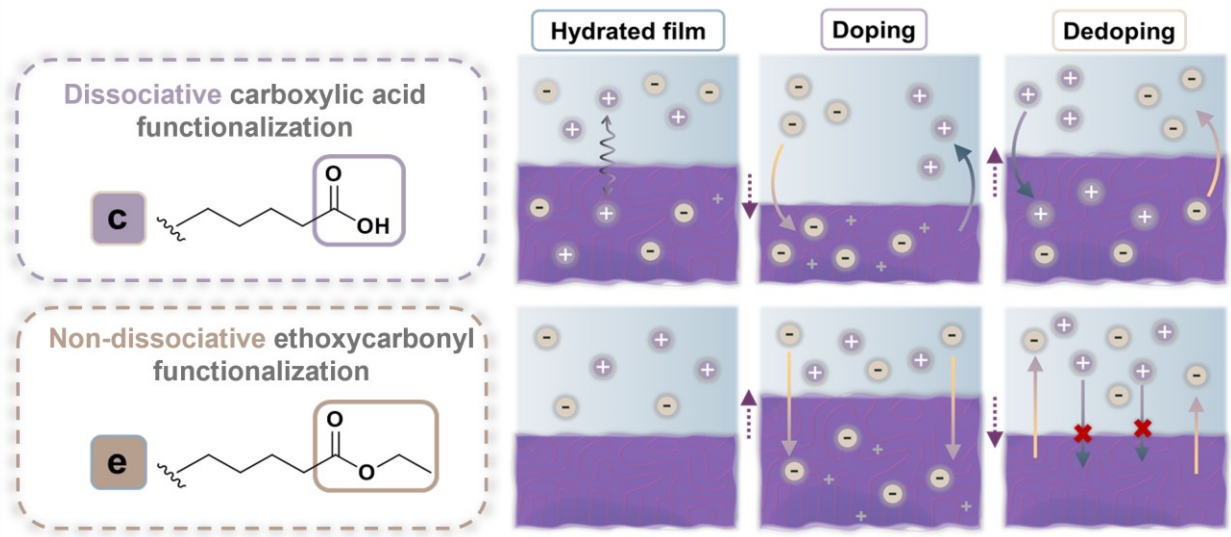

Abstract

Organic mixed ionic-electronic conductors (OMIECs) have garnered significant attention due to their capacity to transport both ions and electrons, making them ideal for applications in energy storage, neuromorphics, and bioelectronics. However, charge compensation mechanisms during the polymer redox process remain poorly understood, and are often oversimplified as single-ion injection with little attention to counterion effects. To advance understanding and design strategies toward next-generation OMIEC systems, we investigate a series of p-channel carboxylated mixed conductors. Varying side-chain functionality, we uncovered distinctive swelling character during electrochemical doping/dedoping with model chao-/kosmotropic electrolytes. Carboxylic acid functionalized polymers demonstrate strong deswelling and mass reduction during doping, indicating cation expulsion, while ethoxycarbonyl counterparts exhibit prominent mass increase, pointing to an anion-driven doping mechanism. For the first time, by employing *operando* grazing incidence X-ray fluorescence (GIXRF), we reveal that the carboxyl functionalized polymer engages in robust cation interaction, whereas COOEt functionalization shifts the mechanism towards no cation involvement. We demonstrate that cations are pivotal in mitigating swelling by counterbalancing anions, enabling efficient anion uptake without compromising performance. These findings underscore the transformative influence of functionality-driven factors and side-chain chemistry in governing ion dynamics and conduction, providing new frameworks for designing OMIECs with enhanced performance and reduced swelling.

1. Introduction

Organic mixed ionic-electronic conductors (OMIECs)[1] are an emerging class of organic semiconductors capable of simultaneously transporting ionic and electronic charge with potential for applications in the realms of energy storage,[2] neuromorphics,[3] and organic bioelectronics.[4,5] These materials are capable of volumetric doping, allowing anions, cations, and solvent to be dynamically drawn into and expelled from the film electrochemically. Moreover, the functionality and selectivity can be tuned by tailoring polymer structure and morphology. These interactions are particularly important at the atomic level where the underlying solvation and coordination environments under confinement are of critical importance. While volumetric doping allows for creation of materials with high charge densities, this property creates new challenges. At the atomic level, the transport of charge and ionic species results in dimensional changes and rearrangements that impact the local self-assembly of the polymers in both reversible and irreversible ways. These changes can impact the long-range continuity of electronic transport pathways and lead to macroscopic strain, cracking, and delamination of active layers, reducing the lifetime of devices.[6–8] While progress has been made developing materials and optimizing devices, a fundamental understanding of how to modulate the activity of both anionic and cationic species in these mixed conductors is lacking.

Developing design rules that enable simultaneous tuning of ion-polymer interactions and control of the electronic characteristics is vital to advancing the design strategies for next-generation OMIEC systems. The current / leading synthetic strategy for promoting ion uptake in OMIECs is altering side chain polarity through addition of oligo(ethylene glycol) moieties. Such modification has enabled the successful fabrication of p-channel, n-channel, and ambipolar mixed conductors, leading to advances in the field.[9–14] However, the limited side chain diversity has led to an oversimplified view of charge compensation, often described as anion injection into the film for p-channel doping with little consideration of the counterions. As a result, a detailed understanding of doping mechanisms and charge compensation associated with different side chain chemistry/functionality remains elusive, partly due to the lack of direct measurement of ion composition during electrochemical doping.

Elucidating the compositional changes that occur within the microstructure of OMIECs, particularly through time-resolved characterization, is critical for unraveling the coupling between ionic and electronic charges.[15–17] Efforts have been made in previous studies to investigate the ion composition in OMIECs, although most of these works are based on indirect approaches.[18,19] Flagg *et al*. demonstrated a unique scenario involving a model glycolated polymer, poly(3-{[2-(2-methoxyethoxy)ethoxy]methyl}thiophene-2,5-diyl) (P3MEEMT) in KPF_6, which initially expels cations from the film followed by anion injection.[20] They also noted that an increase in crystallinity may likely restrict cation uptake,[21] yet a fundamental understanding of the factors driving cation uptake is still lacking. There has been some progress understanding the ionic activity and its connection to both compositional and structural changes within these systems *in situ*, particularly with the introduction of the “frit cell” concept as an *in situ* / *operando* methodology.[22] This approach has proven successful in time-resolved structural characterization of OMIECs and has demonstrated its capabilities across several studies.[23–25] In a noteworthy study, Quill *et al*. revealed a self-assembled nanocomposite of an organic semiconductor and ionic liquid, where electrolyte exposure induces side chain redistribution. The observed changes in lamellar spacing, along with ion dimensions and charge neutrality considerations, suggest that cation expulsion likely occurs during the electrochemical oxidation process in p-channel semiconductors.[26] Notably, none of these studies directly demonstrate ion presence within the films, highlighting the critical need for *in situ* investigations to unravel the holistic picture of ion dynamics.

To drive transformative advances in tailoring OMIEC chemistry for improved compositional and structural understanding, we examine how charged functional groups modify ionic activity and charge selectivity using the state-of-the-art p-channel carboxyl-functionalized conjugated polyelectrolyte, poly[3-(4-carboxylbutyl)thiophene-2,5-diyl] in both its protonated form (P3CBT-P; derived from acidified P3KPT (poly(3-potassium-5-pentanoate-2,5-diyl) films) and pristine form (P3CBT). Using complementary *operando* electrochemical quartz crystal microbalance with dissipation monitoring (EQCM-D), we find the ion uptake behavior depends on the cation identity with corresponding changes in viscoelastic properties and mass uptake during electrochemical doping. This behavior is markedly different than the uncharged ethoxycarbonyl substituted material (COOEt), poly[3-(ethyl-5-pentanoate)thiophene-2,5-diyl] (P3EPT). In P3EPT, cation uptake is significantly inhibited, and the material follows the conventional anion uptake pathway, similar to that observed in p-channel glycolated polymers.[27] To look at ion activity within the OMIEC films, we use *operando* grazing incidence X-ray fluorescence (GIXRF) methodology based on the 'frit cell' to directly probe differences in cation uptake within OMIECs during electrochemical cycling, enabling real-time elemental study on the complex ion transport mechanisms in mixed conductive materials. We observe that carboxylic acid functionalized polymers engage in strong cation-polymer interaction, while ester-functionalized variants do not. This study describes a direct way to contrast how side chain chemistry impacts cation-involved p-channel doping mechanisms and their effects on swelling behaviors, and offers new insights into functionality-driven factors in charge compensation and design strategies within OMIEC systems.

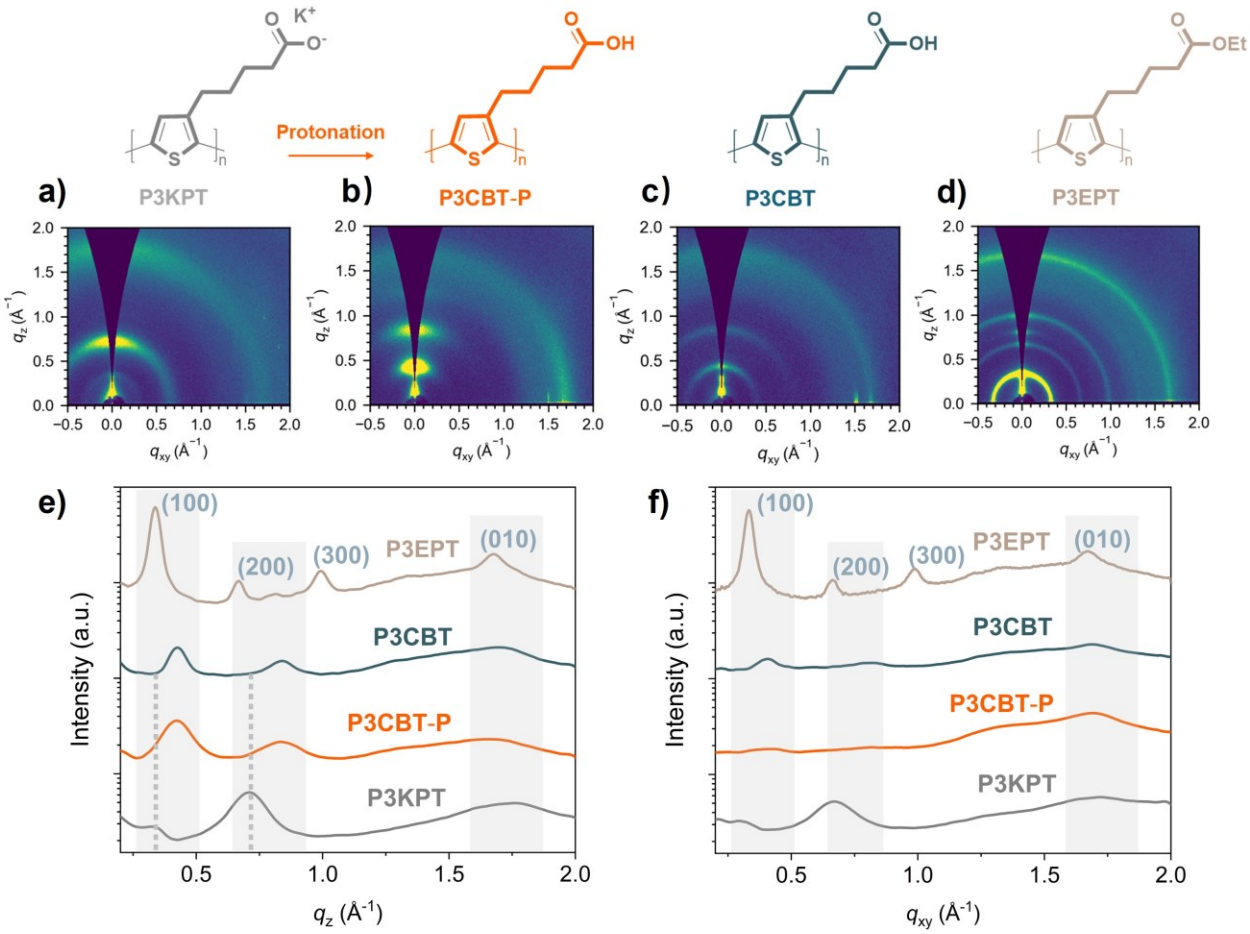

Figure 1: Chemical structures and their corresponding two-dimensional grazing incidence wide-angle x-ray scattering (GIWAXS) patterns for the carboxylated polymers used in this study, from left to right are, **a)** water-soluble potassium carboxylate salt precursor poly[(3-potassium-5-pentanoate)thiophene-2,5-diyl], P3KPT, **b)** protonated P3KPT, namely P3CBT-P derived from as-cast P3KPT, **c)** pristine P3CBT, and **d)** P3EPT respectively; **e)** Out-of-plane and **f)** in-plane GIWAXS profile of P3KPT, P3CBT-P, P3CBT and P3EPT films, respectively.

2. Results and Discussion

In this study, films of the protonated form of P3KPT, namely P3CBT-P, were prepared *via* acidification of spray coated P3KPT films, as described previously.[28,29] Pristine P3CBT films were obtained from spray cast solutions of P3CBT dissolved in dimethyl sulfoxide (DMSO) and served as a control for structural and compositional comparison. P3EPT films were spray cast from dichlorobenzene (DCB) solutions to provide an additional control for assessing the impact of the side chain functionality. Spray casting was selected for this study because it is advantageous for achieving uniform, controlled thickness films on complex surfaces with material efficiency, in addition to being a scalable, high throughput technique.[30–33]

The molecular arrangement and packing characteristics of the polythiophenes were investigated using grazing incidence wide-angle X-ray scattering (GIWAXS) (data are summarized in **Table S1**). A comparison of the film morphology before and after acid treatment (**Figure 1a,b**) shows a structural reorganization due to the K-to-H conversion and a marked change in the crystallite texture. The lamellar spacing of the starting P3KPT film is $d = 1.84_{(100)}$ nm ($q_z = 0.34_{(100)}$ Å^{-1}) and the $\pi - \pi$ stacking distance is $d = 0.37_{(010)}$ nm ($q_{xy} = 1.70_{(010)}$ Å^{-1}). After the conversion, the P3CBT-P film has a lamellar spacing of $d = 1.46_{(100)}$ nm, while the $\pi - \pi$ distance remains relatively unchanged. The change in lamellar spacing is expected since the ion exchange likely results in a volumetric change, and no measurable change in lattice spacing in the $\pi - \pi$ stacking is observed. Similar observations were reported for PEDOT:PSS analogues, where the results were primarily attributed to a reduced molar ratio of styrene sulfonate to EDOT units, achieved through acid-assisted washing that decreases PSS- content. Excess PSS- often acts as a barrier, disrupting the close stacking and alignment needed for crystallinity.[34] As compared to the directly cast P3CBT film (**Figure 1c**), the two step conversion process appears to induce edge-on texturing of the film crystallites. The impact of this conversion on the internal porosity is yet unknown, although it may improve the ion accessibility within the conductive network *via* increasing the effective electrochemical interface.[35,36] Next, the composition of films generated *via* K-to-H conversion was investigated using low energy ion scattering (LEIS), an advanced technique that derives compositional information through ion-etching.[37] Potassium was detected in the protonated film after etching approximately 40 nm into the film, which likely contributes to the formation of more amorphous regions[38] and as suggested by the Raman spectrum, compared to pristine P3CBT (see **Figure S1**). The P3EPT film morphology (**Figure 1d**) appears noticeably expanded based on the lamellar spacing of $d = 1.84_{(100)}$ nm with a similar $\pi - \pi$ spacing of $d = 0.38_{(010)}$ nm. This lamellar expansion is expected due to the increased volume of the ethoxycarbonyl group. However, we note the presence of a unique scattering feature in the out-of-plane direction at $q_z = 0.81$ Å^{-1}, making direct comparison of P3EPT to the carboxylated materials difficult (**Figure 1e**). Moreover, the appearance of a sharp structural feature at $q_{xy} = 1.67_{(010)}$ Å^{-1} in P3EPT that appears in-plane and is absent in carboxylated polymers (**Figure 1f**), likely indicates a higher overall crystallinity. To further reveal the crystallinity among the series, Warren-Averbach analysis and differential scanning calorimetry revealed that the ester-functionalized polythiophene exhibits greater long-range order along the lamellar stacking direction and higher crystallinity than the carboxylated counterparts (see **Table S2** and **Figure S2**).

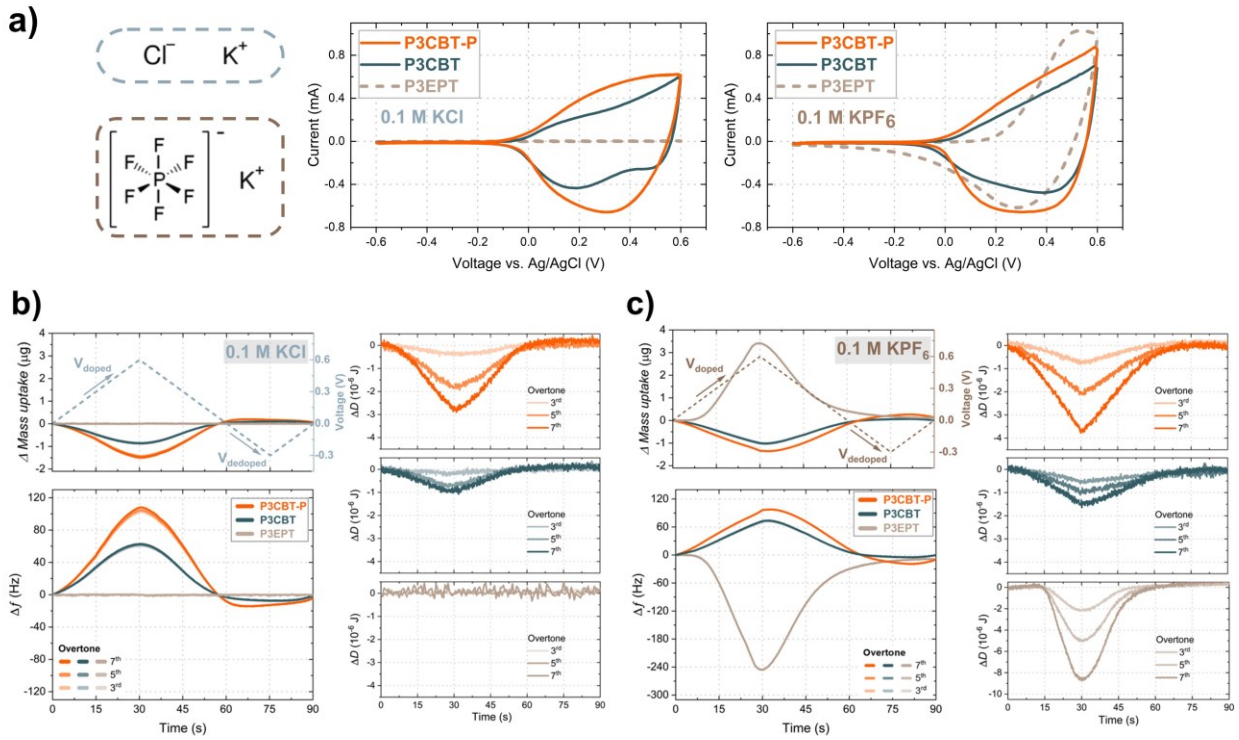

Figure 2: **a)** Chemical structure of electrolytes used in this work, potassium chloride (KCl) and potassium hexafluorophosphate (KPF_6). Cyclic voltammetry was performed at a rate of 50 mV s^{-1} in 0.1 M KCl and 0.1 M KPF_6 for P3CBT-P (orange), P3CBT (cyan) and P3EPT (light brown) with films cast on ITO slides. Comparison of EQCM-D data during the 6th CV cycle from 0 to 0.6 V to -0.3 V *vs* Ag/AgCl. **b)** mass change/voltage profile, and frequency changes for 3rd, 5th and 7th overtones, and dissipation variation in 0.1 M KCl; **c)** mass change/voltage profile, and frequency changes for 3rd, 5th and 7th overtones, and dissipation variation in 0.1 M KPF_6. All the films used in this study were spray cast to about 250 nm, and their corresponding charge accumulation is shown in **Figure S5**

The electrochemical characteristics of the carboxylated polymers and P3EPT were studied using cyclic voltammetry in both 0.1 M KCl and KPF_6 (**Figure 2a**). In 0.1 M KCl electrolyte, both COOH-functionalized polymers demonstrate unipolar p-channel doping; notably, P3CBT-P reaches an earlier onset potential and greater charge accumulation compared to P3CBT. The ester-functionalized polymer is electrochemically inactive under chloride conditions; however, substitution of the anion with a hydrophobic/chaotropic anion such as PF_6^-, which is known to enhance electrochemical performance in various polythiophene systems,[21,39,40] yields interesting results. As depicted in **Figure 2a**, both COOH-functionalized polymers show marginal performance improvement in KPF_6 compared to the chloride containing electrolyte, with P3CBT-P still outperforming pristine P3CBT. This result is perhaps atypical, as most of the reported glycolated polymers exhibit either a dramatic performance difference or an earlier shift in onset potential. More significantly, P3EPT demonstrates substantial enhancement in performance with PF_6^-, exhibiting unipolar p-channel doping. Clearly, COOH and COOEt groups interact with ions very differently, where substitution of a kosmotropic anion (water-structure-forming) with a chaotropic alternative (water-structure-breaking) provides for limited improvement for carboxylic acid functionalization but exhibits dramatic differences in the case of ester substitution.

"Passive" swelling characteristics of the carboxylated polymers in aqueous electrolytes was examined by quartz crystal microbalance with dissipation monitoring (QCM-D) without applying bias. The swelling of

polymer thin films of various thicknesses was measured in 0.1 M KCl electrolyte and compared to a reference sample in air.[41] Minimal thickness change was observed for the P3EPT film (~1.4%), resulting in an almost negligible volumetric change. In contrast, the P3CBT-P and P3CBT films demonstrated significantly more swelling, at 16.8%, and 7.8%, respectively (see **Figure S3** and **Table S3**). Contact-angle measurements provided additional evidence (full comparison presented in **Figure S4,** with all electrolytes), with P3EPT being the most hydrophobic of the series (~78º), followed by P3CBT (~63º), and P3CBT-P (~55º), which aligns with the passive swelling results. This substantial difference is attributed to the more hydrophilic nature of carboxylic acid *vs.* ethoxycarbonyl functional groups and suggests that P3CBT-P is more hydrophilic or amorphous compared to pristine P3CBT.

The "active" swelling behavior was investigated by coupling QCM-D with an electrochemical module during cyclic voltammetry, which leads to ion/water injection/ejection into the bulk of the film structures. **Figure 2b,c** displays the net mass and frequency change during oxidation and reduction for one cycle with a scan rate of 20 mV s^{-1} in 0.1 M KCl and KPF_6 respectively, and their charge accumulation is presented in **Figure S5**. Surprisingly, as the potential starts from 0 to 0.6 V (indicated as doping), the net mass for both P3CBT-P and P3CBT initially *decreases*; and as the potential is swept back from 0.6 V to 0 V, the net mass restores to its baseline level. Subsequent dedoping (from 0 to -0.3 V) results in a slight *increase* in mass. This indicates that doping primarily occurs *via* cation expulsion and this behavior predominately modulates mass change through electrochemical doping. P3CBT-P undergoes a higher degree of mass change than P3CBT, indicating higher ion/water uptake in agreement with the passive swelling results. This process is likely intricately governed by the crystallinity and hydrophilicity of the polymer.

Figure 2b,c also illustrates the time-dependent dissipation change during CV in 0.1 M KCl and KPF_6: P3CBT-P and P3CBT exhibit *increased rigidity* evidenced by decreased dissipation, aligning with the mass reduction, with P3CBT-P exhibiting a more viscoelastic feature compared to pristine P3CBT. Both polymers exhibited more changes in dissipation in KPF_6 over KCl, likely indicating more K^+ diffused out of the film in KPF_6 during doping. Further comparison of P3CBT-P in both KCl and KPF_6 are shown in **Figure S6**, where a hysteresis effect is observed in KPF_6 starting at around 0.3 V and across the dedoping range (0.6 V to -0.3 V), indicating different mass kinetics induced by different counter ion pairs during the doping/dedoping phase. P3EPT exhibits no obvious ion flux in or out of the film in KCl, aligned with the CV data in **Figure 2a**, resulting in no observable changes in mass or dissipation. Conversely, under KPF_6 conditions, P3EPT displayed a predominate anion uptake mode, evidenced by a net increase in mass during doping. Comparative analysis of mechanical dissipation, shown in **Figure 2c**, reveals that P3EPT densified despite the net mass increase. Typically, such a decrease in dissipation energy was previously observed only in glycolated polymers with chaotropic anions (e.g. PF_6^- and $TFSI^-$), where a decrease in dissipation is typically attributed to mass *decrease* induced by cation expulsion.[20,25] The ester functionalized polymer contradicts this rationale. Therefore, we hypothesize that changes in dissipation are more closely associated with the type of ion and ion-water-polymer interaction rather than mass change in ester-functionalized polymer film, where chaotropic ions (such as PF_6^-) will increase mechanical stiffness of the polymer through behavior akin to ionic crosslinking with minimal solvent uptake.[42,43] Furthermore, all polymers exhibit a clear thickness-dependent effect (as shown in **Figure S7 and S8**) – thicker films (~250 nm) uptake/repel more ions with greater dissipation changes than thinner films (~150 nm) – underscoring the necessity of reporting film thickness in EQCM-D for comparison.

Encouraged by the active swelling results, we further elucidate the complete hydration mechanism by including the initial stabilization process with 5 cycles of CV for both types of functionalized polymers, as shown in **Figure S9**. Interestingly, the COOH polymer required one to two cycles to stabilize, depending on thickness, with dedoping being the major phase during which the polymer experienced an irreversible cumulative mass retention. This suggests that COOH polymer films undergo significant hydration by cation

hydration shells under both KCl and KPF_6 conditions.[44,45] These findings are consistent with the CV results presented in **Figure 2a**, where switching only anions resulted in minimal improvement in mixed conduction. This underscores the importance of considering the chaotropic/kosmotropic nature of both cations and anions when interacting with carboxyl group, indicating that the co-ion properties must be considered.[46] Conversely, the COOEt polymer demonstrated similar behavior to other p-channel polythiophene analogues, showing reversible mass change and minimal retention, suggesting little to no cation involvement or hydration. [47]

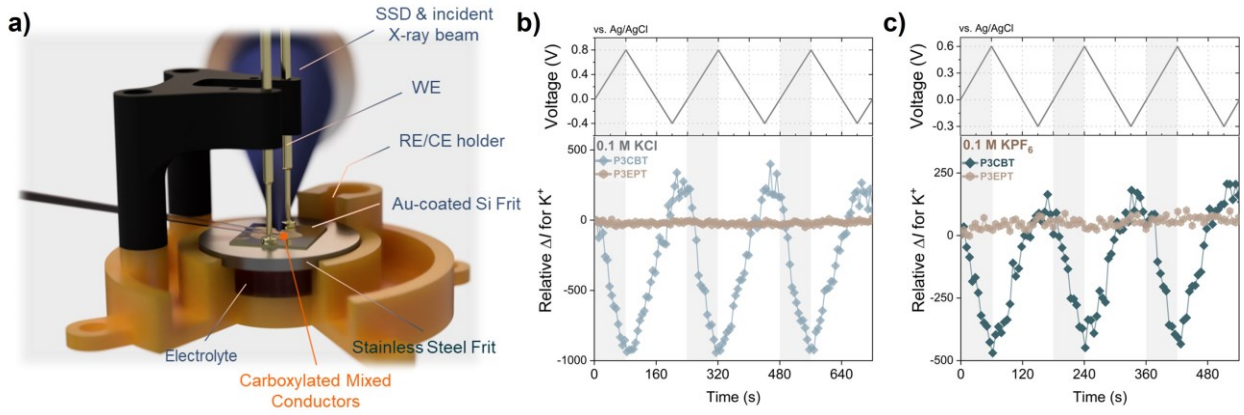

Figure 3: **a)** Schematic of the electrochemical frit cell used for *operando* GIXRF measurements. XRF spectra of relative intensity change for potassium cation in carboxylic acid functionalized and ester functionalized polymers in **b)** 0.1 M KCl, and **c)** 0.1 M KPF_6 during CV cycles at a rate of 10 mV s^{-1}.

To investigate the ion composition within cycling devices, the X-ray fluorescence (XRF) signal was collected in *operando* using the recently developed frit electrochemical cell.[22,26] Analogous to conventional visible light fluorescence, X-ray fluorescence (XRF) uses high energy X-rays to excite X-ray emission with energies that are unique to each element. This technique has been previously applied in OMIEC materials to track macroscopic lateral ion transport and mobility in electrochromic moving front experiments.[48] A significant challenge using XRF to study conventional thin-film OMIEC devices is the long penetration length of the hard X-ray source and the considerable background signals of ions in the bulk electrolyte. Thus, an experimental geometry that limits the direct interaction of the hard X-ray source to the OMIEC material alone and minimizes this interaction with the bulk electrolyte is critical. To limit X-rays to the OMIEC thin film, we combined XRF with the grazing incidence X-ray frit electrochemical cell to enable *operando* measurements as shown schematically in **Figure 3a**. In this setup, an OMIEC sample is transferred on top of a gold coated, porous silicon membrane which serves as both the working electrode and current collector, respectively. To make electrical contact with this top gold surface and avoid bending of the porous silicon substrate, the porous silicon is placed on top of a polished stainless-steel frit and the electrical connection to the gold top layer is made using spring-loaded pogo pins. An electrolyte reservoir and an Ag/AgCl electrode are situated below the sample and capillary action draws electrolyte through frit and both porous silicon to wet the OMIEC sample. This creates a fully functional device with a solid-vapor interface above the OMIEC layer and a liquid-solid interface below. The Ag/AgCl electrode functions as both the reference and counter electrode. As previously shown,[22] a grazing incidence X-ray beam interacts primarily with the OMIEC layer with minimal interaction with the bulk electrolyte within the pores. We note the XRF is generally probing the bulk composition within OMIEC layer for the experiments herein. Self-absorption of the fluorescing X-rays is not believed to be a significant issue. Additionally, a population of sorbed ionic species within the OMIEC device may be present although these ions may not participate in the electrochemical

activity of the device. The full setup and operational details are provided in Supporting Information and **Figure S10**, and notably, the study focuses on the dynamic changes of K^+, with raw spectra presented in **Figure S11** and **S12**. Changes in the potassium K-edge XRF signal (~3.4 keV) offer the most direct access to monitoring the p-channel electrochemical doping/dedoping process. As illustrated in **Figure 3b,c,** the XRF spectra of the carboxylic acid functionalized and ethoxycarbonyl functionalized polymers were measured under 0.1 M KCl and KPF_6, respectively, during three CV cycles. In the COOH functionalized polymer, the relative intensity of K^+ significantly decreased when swept within the range of doping potential (0 V to 0.6 V/0.8 V) in both electrolytes, and then returned back to the original intensity at 0 V and increased further in the dedoping potential range (-0.3 V/-0.4 V). In contrast, COOEt-functionalization results in minimal changes in K^+ intensity, suggesting that there is no interaction between the ester group and cations within the film.

Combining the knowledge of the potassium signal with the mass changes leads to additional insights into the cation-polymer interaction (**Figure S13**), where the 7th overtone of the EQCM signal for P3CBT and P3EPT in 0.1 M KCl are presented. V_{oc} represents the film's voltage upon initial electrolyte exposure (without external bias). A frequency reduction (mass increase) occurs in P3CBT when switching from V_{oc} to 0 V or -0.6 V, indicating cation/water absorption modulated by potential, where P3EPT shows no frequency change, suggesting no cation-polymer interaction. Similar effects of COOH are observed with other aqueous electrolytes, as shown in **Figure S14**, confirming that carboxylic acid functionalization facilitates strong cation-polymer interactions across a range of ion types, including alkali metals (Li, Na, K, Cs etc.) and non-metallic cations such as *tetra*-n-butylammonium, unlike glycolated polymers, which exhibit cation expulsion only under specific conditions.[19,20,25] These data provide direct evidence that cations are actively incorporated into the COOH-functionalized film upon electrolyte exposure, undergoing dynamic ejection and injection during doping and dedoping cycles, but COOEt functionalization does not facilitate ion interactions, indicating the absence of such cation transport.

Complementary spectroscopic analysis further provides deeper understanding of the oxidation state and ionic/polaronic characteristics of carboxylated mixed conductors. *Ex-situ* UV-Vis spectra reveal that both carboxylic acid polymers in the dry state display a polaron band around 900~1000 nm, indicating polaron formation under ambient condition (**Figure S15**). This serves as direct evidence of internal charge compensation or a self-doping effect driven by the ionized COOH functionality, which undergoes partial deprotonation. This resulting ionization facilitates self-doping within the polymer, positively polarizing the conjugated backbone with holes.[49,50] In contrast, the non-ionized ethoxycarbonyl functionalized polymer does not exhibit this feature. Complementary *in-situ* spectroelectrochemistry was performed to investigate cation/anion pairs and oxidation state changes during the electrochemical doping process (**Figure S16**). For p-channel polymers and as supported by previously reported results,[20,28,29] the spectra typically remain unchanged in their dedoped state; and as potential increases cathodically, anion-driven electrochemical doping reduces the 0-1 absorption band while simultaneously enhancing growth of the polaron band (hole injection). For carboxyl functionalization, this behavior is observed immediately upon electrolyte exposure (V_{oc}) in both KCl and KPF_6 condition, with a notably higher polaronic intensity observed in KPF_6 relative to KCl in both COOH-functionalized polymers. This demonstrates that electrolyte-derived anions are not only incorporated into the polymer but also synergistically interact with the polymer to enhance the polarization of the conjugated backbone, suggesting the presence of a cation/anion/hole complex in the hydrated film. Further potential reductions to 0 V and -0.6 V result in a gradual increase in cation density with minimal or no anion presence, leading to the disappearance of those changes, indicating that cations do not contribute to either vibronic bands or polaron formation. For ethoxycarbonyl-functionalized polymers, this behavior is not observed, suggesting that cation/anion pairs are absent in the film, both at open circuit potential and in the dedoped state.

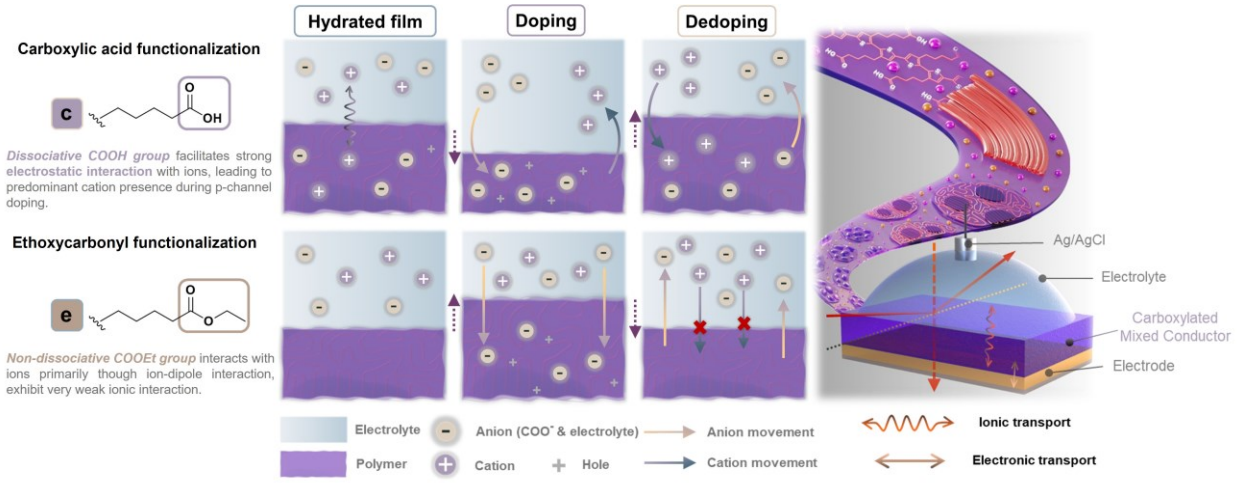

Figure 4: Schematics integrating results from EQCM-D, operando GIXRF, and spectroelectrochemistry measurements, illustrating the mechanism of carboxylated mixed conductors during hydration, and electrochemical doping/dedoping. The top row highlights carboxylic acid functionalization, and the lower panel refers to ethoxycarbonyl functionalization. Figure on the right, adapted from [28], demonstrates how different operando characterization techniques uncover the mechanism of electrochemical redox behavior.

Together, the presented data supports the following proposed doping mechanism for electrochemical doping/dedoping of carboxylated mixed conductors as shown in **Figure 4**. For carboxylic acid functionalization, prior to initiation of electrochemical doping/dedoping initial contact with the electrolyte leads to swelling and hydration of the film, engaging cations/anions/holes complexes in the film. Upon application of an oxidative bias, substantial migration of cations out of the film, accompanied by anion influx and hole injection, is observed. The process is predominately driven by cation flux, resulting in film *de*swelling. As the potential reverses toward the dedoping phase, this dynamic inverts: cations re-enter the film to neutralize intrinsic carboxylate anion as holes are extracted, while electrolyte-derived anions depart. In the case of ethoxycarbonyl functionalization, the initial phase exhibits negligible hydration and swelling, and the system is devoid of any cation-anion pair within the film. During the doping phase, substantial influx of anions occurs as holes are injected, leading to significant swelling and stiffening of the polymer. As the potential reverses, these injected anions are expelled, restoring the polymer to its original, minimally hydrated and largely ion-free state.

Furthermore, the bidirectional cation-anion transport associated with carboxylic acid functional group and their role in modulating the swelling/deswelling behaviors of polymers was scrutinized, particularly in comparison to a glycolated polymer model, poly(3-[2-[2-(2-methoxyethoxy)ethoxy]ethyl]thiophene)−2,5-diyl) (P3MEEET) in a 0.1 M KCl electrolyte as shown in **Figure S17**. Interestingly, the oligo ethylene glycol functionality also exhibits minor cation expulsion at the initial phase of doping. The participation of both cationic and anionic species in the COOH polymer, with a pronounced cation predominance during electrochemical doping, leads to markedly different doping behaviors: the carboxylic acid functionalized material undergoes *de*swelling and reduction in mass with a nearly negligible increase in rigidity, while the glycolated alternative experiences significant swelling and mass increase, with extensive plasticizing effect by the electrolyte. Unlike esterified and glycolated polythiophenes, which primarily exhibit volume *increases* driven by predominant single-ion (specifically anion in the cases discussed here) injection with minimal cation involvement, COOH-functionalized polymers enable *pre-doping cation infiltration*. This is subsequently followed by *cation expulsion* and *anion influx* during doping, resulting in a volume response dominated by deswelling rather than expansion. These results indicate that the simultaneous engagement

of both ions orchestrate a dual pathway, effectively regulating ion dynamics and mitigating undesirable swelling during electrochemical (de)doping. Counterions (cations in p-channel polymers) are essential in counterbalancing the influx of doping ions (anions in p-channel polymers), and thus may help maintain structural integrity and functional performance by limiting negative impacts of swelling/deswelling during cycling.[28] This yields a consistent deswelling response across different electrolytes, even with substantial molecular weight differences (e.g., Cl^- *vs* PF_6^-), underscoring the critical influence of cation-polymer interactions. Thus, aliphatic COOH functionalization offers a promising approach to achieving "low swelling" by concurrently enabling counterion transport and facilitating adequate doping ion uptake. This approach supports the reversible modulation of current, mass, and mechanical properties during electrochemical cycling, ensuring consistent functionality and minimizing unwanted dimensional changes in model electrolytes (**Figure S18**). *This finding provides new insights into the design and development of organic ionic-electronic mixed conductors with lower swelling or even non-swelling characteristics without sacrificing performance.*

We emphasize that side chain functionality significantly impacts ion uptake during the electrochemical doping/dedoping process. Carboxylic acid groups, being highly polar, can dissociate into a carboxylate anion and a proton. This deprotonation, driven by the acid dissociation constant, enables strong electrostatic interactions with ions. Notably, even carboxylic acids with limited solubility in aqueous environments can dissociate at the polymer-electrolyte interface, enabling the coexistence of ion-ion and ion-dipole interaction, underscoring the crucial role of molecular interactions at the solid-liquid interface. In contrast, esters, being less polar than carboxylic acids, do not ionize or carry a charge under typical conditions. As a result, esters can only engage in weak ion-dipole interactions and lack the capacity to engage in electrostatic interactions with cations as carboxylic acids do. The presence of an ethyl cap not only adds significant steric hindrance, but also amplifies the hydrophobic character, intensifying the ionophobic effect, especially under kosmotropic ions. These distinctions in polarity and ionization behaviors underscore the broader difference in how functional groups interact with ions during p-channel electrochemical doping/dedoping processes.

3. Conclusion

In conclusion, this study provides a comprehensive understanding of the electrochemical doping/dedoping mechanism in a family of carboxylated polythiophenes with model chao- / kosmotropic electrolytes, offering real-time insights into the complex interplay between ion uptake and polymer functionality. The dissociative nature of COOH facilitates strong cation-polymer interactions, allowing both cations and anions to participate in the charge compensation, with ion uptake modulated by polymer processing condition. Conversely, the COOEt-functionalized variant exhibits a conventional anion-driven uptake without cation-polymer interaction, highlighting the pivotal role of side chain chemistries in governing ion activity. Notably, we reveal for the first time that cations can play a crucial role in swelling control by counterbalancing anions while supporting efficient anion uptake for p-channel doping, which provides insight into designing new carboxylated mixed conductors with minimal or non-swelling characteristics without compromising performance. The results illustrate the importance of viewing and understanding OMIECs as an integrated polymer-ion-water system rather than focusing solely on the intrinsic material properties. This requires a shift in characterization approaches, employing active *in situ* techniques to capture the full range of structural, compositional, and property-related intricacies under different operating conditions. This study serves as a compelling example of the necessity for multimodal characterization to thoroughly understand and optimize the inherent complexities in OMIEC systems, offering deeper insight into their conduction mechanisms.

4. Experimental Section

Carboxylated Mixed Conductor Solution and Film Preparation: P3K(Pe)T (poly(3-potassium-5-pentanoate)thiophene-2,5-diyl), Mw = 28 kDa, PDI = 2.0, Batch # BLS26-51), P3CBT (poly(3-(4-carboxylbutyl)thiophene-2,5-diyl), Mw = 39 kDa, PDI = 2.3, Batch # PTL39-74), P3EPT (poly(3-(ethyl-5-pentanoate)thiophene-2,5-diyl), Mw = 39 kDa, PDI = 2.3, Batch # PTL37-60), P3MEEET (Poly(3-[2-[2-(2-methoxyethoxy)ethoxy]ethyl]thiophene)−2,5-diyl), Mw = 18 kDa, PDI = 1.6, Batch # BLS26-79)) were purchased from Rieke Metals Inc. *p*-Toluenesulfonic acid monohydrate (pTsOH-H2O, 98%, Sigma-Aldrich), potassium chloride (99.9%, Sigma-Aldrich), potassium hexafluorophosphate (99.9%, Sigma-Aldrich), dimethyl sulfoxide (99.9%, Sigma-Aldrich), 1,2-dichlorobenzene (99%, Sigma-Aldrich), acetone (99.5%, Sigma-Aldrich), methanol (99.8%, Sigma-Aldrich), and isopropyl alcohol (99.5%, Sigma-Aldrich) were used as received. Deionized (DI) water with a resistivity of 18.2 mΩ cm was obtained using an Aries water purification system (ARS-105). P3CBT-P thin films were fabricated following the previously reported acidification method[28,29] by dissolving carboxylate salt into water at a concentration of 2 mg mL^{-1} followed by deposition and acidification to COOH. P3CBT was dissolved in dimethyl sulfoxide (DMSO) at a concentration of 2 mg mL^{-1} , and P3EPT was dissolved in 1,2-dichlorobenzene (DCB) at a concentration of 2 mg mL^{-1}. All polymer solutions were stirred at room temperature overnight. The resulting polymer solutions were then spray-cast using an Iwata Eclipse HP-CS airbrush (gravity feed) and heated to 80°C for P3CBT-P and 130°C for P3CBT and P3EPT. The films were cast onto various substrates, including glass, indium tin oxide (ITO) coated glass (Delta Technologies, resistivity = 8–12 Ω sq^{-1}) for *in situ* measurements, gold sensors for quartz crystal microbalance with dissipation (QCM-D) (QX-338 Ti-Au QCM sensor, active area of 0.785 cm^2), and silicon for grazing incidence wide-angle X-ray scattering (GIWAXS) characterization.

Polymer Microstructural Analysis: Grazing incidence wide angle X-ray scattering (GIWAXS) was performed at the Stanford Synchrotron Radiation Lightsource (SSRL) beamline 11-3, using an area detector (Rayonix MAR-225) with an incident energy of 12.7 keV. The sample-to-detector distance was 315.9 mm, calibrated using a LaB_6 polycrystalline standard. The incidence angle was set to 0.12°, slightly above the critical angle, to sample the full film depth. All X-ray measurements were conducted in a He chamber to minimize air scattering and prevent beam damage to the samples. Raw data was normalized by detector counts and analyzed using the custom python code.[51]

Low Energy Ion Scattering (LEIS): LEIS measurements were performed using an IONTOF Qtac100 to show composition information for the carboxylated mixed conductors. The analysis beam was 3 keV He^+ operated at a current of 10 nA and a raster area of 0.5 x 0.5 mm. The sputter beam was 0.5 keV Ar^+ and operated at a current of 100 nA and a raster area of 1.0 x 1.0 mm. Each level of the sputter depth profile consisted of a $1x10^{16}$ He^+ cm^{-2} and $2.5x10^{16}$ Ar^+ cm^{-2}, corresponding to a depth of approximately 5 nm per cycle. To mitigate charging of the surface layers, charge neutralization was performed using a low energy electron beam.

Differential Scanning Calorimetry (DSC): DSC was performed using a TA Instruments Q2000 Calorimeter. DSC was performed on each sample with a heat-cool-heat sequence. The temperature sweep started at room temperature with a ramp rate of 10 ˚C/min up to 250 ˚C; The sample was cooled down to -80 ˚C at a ramp rate of 100 ˚C/min. Then, the sample was heated at 10 ˚C/min to 250 ˚C. All slopes were reported from the third cycle and determined using built-in features of TA Instrument's Universal Analysis software.

Contact Angle Measurement and Thickness Measurement: Contact angle measurements were performed on a ramé-hart Model 260 Standard Contact Angle Goniometer/Tensiometer with DI water and electrolyte on polymer-coated glass. Thickness measurements were performed using an 3D optical profilometer/interferometer system ZeGage™ Pro.

Cyclic voltammetry (CV): CV was conducted by using an AMETEK PMC 200 Potentiostat/Galvanostat and a three-electrode setup. The working electrode (WE) was prepared by spray-coating the conjugated polymer films onto ITO-coated glass slides (Delta Technologies, resistivity = 8–12 Ω sq^{-1}). A platinum counter wire was used as the counter electrode (CE), and a standard Ag/AgCl electrode (3 M aqueous KCl inner solution, BASi) was used as the reference electrode (RE). 0.1 M KCl (*aq*) and KPF_6 (*aq*) solution was used as the electrolyte. To ensure accurate measurements, all electrolytes were degassed under argon flow for 15 min both prior to and during the measurement process. The scans were recorded at a scan rate of 50 mV s^{-1} with a step size of 2 mV.

Quartz Crystal Microbalance with Dissipation Monitoring (QCM-D): Passive swelling measurements were conducted with a Q-Sense Explorer Analyzer. First, the response of the bare Ti/Au sensors were recorded using QCM-D in air condition, followed by measurements after injection of 0.1 M KCl (*aq*) electrolyte into the chamber. These control measurements resulted in significant shifts in frequency and dissipation due to density differences between the media, which were excluded from the swelling percentage calculation. The sensors were then removed, and the conjugated polymer films were spray coated directly onto the same sensors for P3CBT and P3EPT, additional acidification steps are performed to make P3CBT-P thin film as previously described.[28,29] The absolute difference in frequency between the bare sensor and the Ti/Au/Polymer coated sensors was compared using the "stitched data" function of Q-Soft software. This function accounted for density differences and allowed for direct determination of mass changes per unit area using the Sauerbrey equation (**Equation 1**). The calculated mass changes were then converted to thickness changes, considering the sensor area and assuming a density of 1 g-cm^{-3} for the polymers in different states (dry and wet).

$$\frac{\Delta m}{A} = \frac{-17.7}{n}\Delta f_n \quad \textbf{Equation 1}$$

Electrochemical Quartz Crystal Microbalance with Dissipation Monitoring (EQCM-D): Active swelling measurements under electrochemical doping/dedoping were performed using a Gamry interface 1010B coupled with Q-sense electrochemistry module (QEM401, Biolin Scientific). The three-electrode setup comprised an Ag/AgCl reference electrode, a Pt counter electrode and a polymer coated gold sensor (QX-338 Ti-Au QCM sensor, active area of 0.785 cm^2) as working electrode. All polymers were equilibrated by five cyclic voltammetry cycles from -0.3 V to 0.6 V at a scan rate of 20 mV s^{-1}. Frequency data and dissipation shifts were collected on 3rd, 5th, and 7th overtone for all polymers on QSotf401, and the data is further analyzed and fitted by D-find software.

Operando Grazing incidence X-ray fluorescence (GIXRF): *Operando* GIXRF spectra were measured at fluorescence mode using Vortex silicon draft detector (SDD) with an incident energy of 11.6 keV to target potassium K-edge. The X-ray beam was focused to a size of 20 µm (vertical) X 100 µm (horizontal) with an incident angle of 0.12 deg, and the average take-off angle was 8.7 deg above the horizontal plane. Fluorescence was collected at an additional 16 deg behind the normal 90 deg orientation, to avoid the interference from the working electrode (pogo pin). The vertical and horizontal movement of the frit cell were motor-controlled, with a horizontal rocking motion of ±0.4 mm applied throughout the process to minimize beam damage to the film. The XRF detector was positioned 65 to 70 mm away from the sample, and the frit cell was housed in a helium-purged environment, isolated by a 25 µm thin polyethylene sheet, with a bubbler through water to maintain helium separation from the SDD.

The potential control during the *operando* measurement was carried out using a PalmSens4 potentiostat with an Ag/AgCl electrode served as reference and counter electrode and scan rate of 10 mV s^{-1}. A stainless steel frit with 20 µm average pore size were mounted on a sample block to facilitate electrolyte penetration. A silicon frit (MakroPor, thickness 350 µm, pore diameter 8 µm, pore size 12 µm) was purchased from MilliporeSigma. A 5 nm Ti adhesion layer and a 50 nm Au layer were then deposited on the frit surface *via* vapor deposition. The polymer was subsequently float-transferred onto the top of the frit, serving as the working electrode.

In situ Spectroelectrochemitry (SPE): SPE measurements were performed using the same setup as the CV experiment, with a three-electrode configuration in aqueous solution under a nitrogen atmosphere. The working electrode (WE) and reference electrode (RE) were polymer coated ITO and Ag/AgCl, respectively, consistent with the CV experiment described above, with a platinum wire (Gamry) used as the counter

electrode (CE). The experiment was conducted using an Agilent Cary 5000 spectrophotometer with quartz cuvettes having a path length of 1 cm. The polymer thin film was biased under potentiostatic conditions, controlled by Gamry Interface 1010B potentiostat. The film spectra were recorded once WE current reached a steady state which typically required 30 to 60 seconds for each potential step.

Acknowledgements:

The authors appreciate support from the National Science Foundation Grant No. 2408881. In addition, ER, TEG, MS, ZS, SQ, MW, and HL acknowledge partial support from Lehigh University, funds associated with the Carl Robert Anderson Chair in Chemical Engineering, and access to the Lehigh University Institute for Functional Materials and Devices (I-FMD) Materials Characterization Facility (MCF) and Integrated Nanofabrication and Cleanroom Facility (INCF); and BK and YZ appreciate partial support from the Georgia Institute of Technology. Use of the Stanford Synchrotron Radiation Lightsource, SLAC National Accelerator Laboratory, is supported by the U.S. Department of Energy, Office of Science, Office of Basic Energy Sciences under Contract No. DE-AC02-76SF00515. The authors thank Dr. Nathan Wittenberg and Dane Santa for assistance with QCM-D measurement. The authors also thank Dilara Meli, Ruiheng Wu and Joseph Strzalka for highly fruitful discussions and assistance with electrochemical frit cell setup and measurement. The authors extend their gratitude to Ryan Thorpe for his support with low energy ion scattering, and special thanks to Rahul Venkatesh for insightful discussion regarding elemental analysis and XPS depth profiling experiments.

References:

[1] B. D. Paulsen, K. Tybrandt, E. Stavrinidou, J. Rivnay, *Nat Mater* **2020**, *19*, 13.

[2] J. F. Mike, J. L. Lutkenhaus, *J Polym Sci B Polym Phys* **2013**, *51*, 468.

[3] S. T. Keene, C. Lubrano, S. Kazemzadeh, A. Melianas, Y. Tuchman, G. Polino, P. Scognamiglio, L. Cinà, A. Salleo, Y. van de Burgt, F. Santoro, *Nat Mater* **2020**, *19*, 969.

[4] D. T. Simon, E. O. Gabrielsson, K. Tybrandt, M. Berggren, *Chem Rev* **2016**, *116*, 13009.

[5] S. Inal, J. Rivnay, A.-O. Suiu, G. G. Malliaras, I. McCulloch, *Acc Chem Res* **2018**, *51*, 1368.

[6] A. Savva, R. Hallani, C. Cendra, J. Surgailis, T. C. Hidalgo, S. Wustoni, R. Sheelamanthula, X. Chen, M. Kirkus, A. Giovannitti, A. Salleo, I. McCulloch, S. Inal, *Adv Funct Mater* **2020**, *30*, DOI 10.1002/adfm.201907657.

[7] R. Noriega, J. Rivnay, K. Vandewal, F. P. V. Koch, N. Stingelin, P. Smith, M. F. Toney, A. Salleo, *Nat Mater* **2013**, *12*, 1038.

[8] T. Nicolini, J. Surgailis, A. Savva, A. D. Scaccabarozzi, R. Nakar, D. Thuau, G. Wantz, L. J. Richter, O. Dautel, G. Hadziioannou, N. Stingelin, *Advanced Materials* **2021**, *33*, 2005723.

[9] P. Schmode, A. Savva, R. Kahl, D. Ohayon, F. Meichsner, O. Dolynchuk, T. Thurn-Albrecht, S. Inal, M. Thelakkat, *ACS Appl Mater Interfaces* **2020**, *12*, 13029.

[10] A. Giovannitti, D.-T. Sbircea, S. Inal, C. B. Nielsen, E. Bandiello, D. A. Hanifi, M. Sessolo, G. G. Malliaras, I. McCulloch, J. Rivnay, *Proceedings of the National Academy of Sciences* **2016**, *113*, 12017.

[11] L. R. Savagian, A. M. Österholm, J. F. Ponder, K. J. Barth, J. Rivnay, J. R. Reynolds, *Advanced Materials* **2018**, *30*, DOI 10.1002/adma.201804647.

[12] D. Ohayon, A. Savva, W. Du, B. D. Paulsen, I. Uguz, R. S. Ashraf, J. Rivnay, I. McCulloch, S. Inal, *ACS Appl Mater Interfaces* **2021**, *13*, 4253.

[13] A. Giovannitti, C. B. Nielsen, D.-T. Sbircea, S. Inal, M. Donahue, M. R. Niazi, D. A. Hanifi, A. Amassian, G. G. Malliaras, J. Rivnay, I. McCulloch, *Nat Commun* **2016**, *7*, 13066.

[14] R. B. Rashid, W. Du, S. Griggs, I. P. Maria, I. McCulloch, J. Rivnay, *Sci Adv* **2021**, *7*, DOI 10.1126/sciadv.abh1055.

[15] M. Moser, J. Gladisch, S. Ghosh, T. C. Hidalgo, J. F. Ponder, R. Sheelamanthula, Q. Thiburce, N. Gasparini, A. Wadsworth, A. Salleo, S. Inal, M. Berggren, I. Zozoulenko, E. Stavrinidou, I. McCulloch, *Adv Funct Mater* **2021**, *31*, DOI 10.1002/adfm.202100723.

[16] F. Bonafè, C. Dong, G. G. Malliaras, T. Cramer, B. Fraboni, *ACS Appl Mater Interfaces* **2024**, *16*, 36727.

[17] F. Bonafè, F. Decataldo, T. Cramer, B. Fraboni, *Advanced Science* **2024**, *11*, DOI 10.1002/advs.202308746.

[18] R. Wu, B. D. Paulsen, Q. Ma, I. McCulloch, J. Rivnay, *ACS Appl Mater Interfaces* **2023**, *15*, 30553.

[19] T. J. Quill, G. LeCroy, A. Melianas, D. Rawlings, Q. Thiburce, R. Sheelamanthula, C. Cheng, Y. Tuchman, S. T. Keene, I. McCulloch, R. A. Segalman, M. L. Chabinyc, A. Salleo, *Adv Funct Mater* **2021**, *31*, DOI 10.1002/adfm.202104301.

[20] L. Q. Flagg, C. G. Bischak, R. J. Quezada, J. W. Onorato, Christine. K. Luscombe, D. S. Ginger, *ACS Mater Lett* **2020**, *2*, 254.

[21] L. Q. Flagg, C. G. Bischak, J. W. Onorato, R. B. Rashid, C. K. Luscombe, D. S. Ginger, *J Am Chem Soc* **2019**, *141*, 4345.

[22] B. D. Paulsen, A. Giovannitti, R. Wu, J. Strzalka, Q. Zhang, J. Rivnay, C. J. Takacs, *Small* **2021**, *17*, 2103213.

[23] B. D. Paulsen, D. Meli, M. Moser, A. Marks, J. F. Ponder, R. Wu, E. A. Schafer, J. Strzalka, Q. Zhang, I. McCulloch, J. Rivnay, *Chemistry of Materials* **2024**, *36*, 1818.

[24] T. J. Quill, G. LeCroy, A. Marks, S. A. Hesse, Q. Thiburce, I. McCulloch, C. J. Tassone, C. J. Takacs, A. Giovannitti, A. Salleo, *Advanced Materials* **2024**, *36*, DOI 10.1002/adma.202310157.

[25] J. Tropp, D. Meli, R. Wu, B. Xu, S. B. Hunt, J. D. Azoulay, B. D. Paulsen, J. Rivnay, *ACS Mater Lett* **2023**, *5*, 1367.

[26] T. J. Quill, G. LeCroy, D. M. Halat, R. Sheelamanthula, A. Marks, L. S. Grundy, I. McCulloch, J. A. Reimer, N. P. Balsara, A. Giovannitti, A. Salleo, C. J. Takacs, *Nat Mater* **2023**, *22*, 362.

[27] A. Savva, C. Cendra, A. Giugni, B. Torre, J. Surgailis, D. Ohayon, A. Giovannitti, I. McCulloch, E. Di Fabrizio, A. Salleo, J. Rivnay, S. Inal, *Chemistry of Materials* **2019**, *31*, 927.

[28] Z. Sun, B. Khau, H. Dong, C. J. Takacs, S. Yuan, M. Sun, B. Mosevitzky Lis, D. Nguyen, E. Reichmanis, *Chemistry of Materials* **2023**, *35*, 9299.

[29] B. V. Khau, L. R. Savagian, M. De Keersmaecker, M. A. Gonzalez, E. Reichmanis, *ACS Mater Lett* **2019**, *1*, 599.

[30] S. Chen, A. Surendran, X. Wu, S. Y. Lee, M. Stephen, W. L. Leong, *Adv Mater Technol* **2020**, *5*, DOI 10.1002/admt.202000523.

[31] J. F. Ponder, S. A. Gregory, A. Atassi, A. K. Menon, A. W. Lang, L. R. Savagian, J. R. Reynolds, S. K. Yee, *J Am Chem Soc* **2022**, *144*, 1351.

[32] B. T. DiTullio, L. R. Savagian, O. Bardagot, M. De Keersmaecker, A. M. Österholm, N. Banerji, J. R. Reynolds, *J Am Chem Soc* **2023**, *145*, 122.

[33] H. Sun, M. Vagin, S. Wang, X. Crispin, R. Forchheimer, M. Berggren, S. Fabiano, *Advanced Materials* **2018**, *30*, DOI 10.1002/adma.201704916.

[34] S.-M. Kim, C.-H. Kim, Y. Kim, N. Kim, W.-J. Lee, E.-H. Lee, D. Kim, S. Park, K. Lee, J. Rivnay, M.-H. Yoon, *Nat Commun* **2018**, *9*, 3858.

[35] X. Zhang, B. Wang, L. Huang, W. Huang, Z. Wang, W. Zhu, Y. Chen, Y. Mao, A. Facchetti, T. J. Marks, *Sci Adv* **2020**, *6*, DOI 10.1126/sciadv.aaz1042.

[36] Y. Huang, H. Li, Z. Wang, M. Zhu, Z. Pei, Q. Xue, Y. Huang, C. Zhi, *Nano Energy* **2016**, *22*, 422.

[37] C. V. Cushman, P. Brüner, J. Zakel, G. H. Major, B. M. Lunt, N. J. Smith, T. Grehl, M. R. Linford, *Anal. Methods* **2016**, *8*, 3419.

[38] S.-M. Kim, C.-H. Kim, Y. Kim, N. Kim, W.-J. Lee, E.-H. Lee, D. Kim, S. Park, K. Lee, J. Rivnay, M.-H. Yoon, *Nat Commun* **2018**, *9*, 3858.

[39] L. Q. Flagg, R. Giridharagopal, J. Guo, D. S. Ginger, *Chemistry of Materials* **2018**, *30*, 5380.

[40] K. P. Gregory, G. R. Elliott, H. Robertson, A. Kumar, E. J. Wanless, G. B. Webber, V. S. J. Craig, G. G. Andersson, A. J. Page, *Physical Chemistry Chemical Physics* **2022**, *24*, 12682.

[41] J. Surgailis, L. Q. Flagg, L. J. Richter, V. Druet, S. Griggs, X. Wu, S. Moro, D. Ohayon, C. J. Kousseff, A. Marks, I. P. Maria, H. Chen, M. Moser, G. Costantini, I. McCulloch, S. Inal, *Advanced Materials* **2024**, DOI 10.1002/adma.202313121.

[42] S. H. K. Paleti, Y. Kim, J. Kimpel, M. Craighero, S. Haraguchi, C. Müller, *Chem Soc Rev* **2024**, *53*, 1702.

[43] R. Z. Pytel, E. L. Thomas, I. W. Hunter, *Polymer (Guildf)* **2008**, *49*, 2008.

[44] A. Nimkar, F. Malchick, B. Gavriel, M. Turgeman, G. Bergman, T. Fan, S. Bublil, R. Cohen, M. Weitman, N. Shpigel, M. D. Levi, D. Aurbach, *ACS Energy Lett* **2021**, *6*, 2638.

[45] R. Mancinelli, A. Botti, F. Bruni, M. A. Ricci, A. K. Soper, *J Phys Chem B* **2007**, *111*, 13570.

[46] T. Ma, C.-H. Li, R. M. Thakur, D. P. Tabor, J. L. Lutkenhaus, *Nat Mater* **2023**, *22*, 495.

[47] J. Guo, L. Q. Flagg, D. K. Tran, S. E. Chen, R. Li, N. B. Kolhe, R. Giridharagopal, S. A. Jenekhe, L. J. Richter, D. S. Ginger, *J Am Chem Soc* **2023**, *145*, 1866.

[48] R. Wu, X. Ji, Q. Ma, B. D. Paulsen, J. Tropp, J. Rivnay, *Sci Adv* **2024**, *10*, DOI 10.1126/sciadv.adn8628.

[49] Y. Wan, X. Zhang, G. C. Bazan, T. Nguyen, G. Lu, *Adv Funct Mater* **2022**, *32*, DOI 10.1002/adfm.202209394.

[50] P. Bäuerle, K. Gaudl, F. Würthner, N. S. Sariciftci, M. Mehring, H. Neugebauer, C. Zhong, K. Doblhofer, *Advanced Materials* **1990**, *2*, 490.

[51] Y. Pan, J. Huang, D. Gao, Z. Chen, W. Zhang, G. Yu, *Polym Chem* **2021**, *12*, 2471.